

# High-efficiency n-TOPCon bifacial solar cells with selective poly-Si based passivating contacts

Qinqin Wang<sup>a,b,\*</sup>, Hui Peng<sup>a</sup>, Siwen Gu<sup>c</sup>, Kaiyuan Guo<sup>a</sup>, Wangping Wu<sup>b,d</sup>, Bairu Li<sup>a</sup>, Lvzhou Li<sup>a</sup>, Ningyi Yuan<sup>c</sup>, Jianning Ding<sup>a,\*\*</sup>

<sup>a</sup> Institute of Technology for Carbon Neutralization, Yangzhou University, School of Mechanical Engineering, Yangzhou, 225009, PR China

<sup>b</sup> Jiangsu Province Engineering Research Center of High-Level Energy and Power Equipment, Changzhou University, Changzhou, 213164, PR China

<sup>c</sup> Jiangsu Collaborative Innovation Center of Photovoltaic Science and Engineering, Changzhou University, Changzhou, 213164, PR China

<sup>d</sup> Electrochemistry and Corrosion Laboratory, School of Mechanical Engineering, Changzhou University, Changzhou, 213164, PR China

## ARTICLE INFO

### Keywords:

n-TOPCon solar cell  
Selective poly-Si based passivating contacts  
The parasitic absorption  
Secondary LPCVD/Phosphorus diffusion

## ABSTRACT

Improving the conversion efficiency of n-TOPCon solar cell is still a hot topic. The selective poly-Si based passivating contacts (Poly-SEs) are ideal candidates for reducing the parasitic absorption and contact resistivity of n-type silicon solar cells and for providing better current collection. In this work, we used LPCVD and the POCl<sub>3</sub> tube furnace diffusion methods to fabricate the selective poly-Si based passivating contacts, and studied the influences of key process parameters of the SiO<sub>x</sub> layer formation process (the oxidation duration ( $t_{\text{oxidation}}$ ) and the constant pressure duration ( $t_{\text{pressure}}$ )), and POCl<sub>3</sub> tube diffusion process parameters (the POCl<sub>3</sub>-N<sub>2</sub> carrier gas flow rate at the deposition, deposition temperature, drive-in temperature) on the n<sup>+</sup>-poly-Si profiles, recombination current density ( $J_0$ ), contact resistivity ( $\rho_c$ ) of n-TOPCon solar cells. The results showed that the  $t_{\text{oxidation}}$  and  $t_{\text{pressure}}$  had a significant impact on  $J_0$  and  $\rho_c$  which were mainly related to the distribution number of O and Si<sup>4+</sup> content on the growth of the SiO<sub>x</sub> layer. And the influence of the drive-in temperature of phosphorus (P) diffusion process on  $J_0$  value is stronger than that of the deposition temperature, which was mainly related to the chemical passivation of SiO<sub>x</sub> layer induced by P-indiffusion into Si at high temperature. The reduction in the thickness of poly-Si from 110 nm to 30 nm led to an increase in the short-circuit current density ( $J_{sc}$ ) per nanometer of  $\sim 0.0093$  mA/cm<sup>2</sup> per nm. The Poly-SEs were fabricated by 3D printing mask technology and secondary LPCVD/phosphorus diffusion with  $J_0, n^+ \approx 5$  fA/cm<sup>2</sup> (n<sup>+</sup>-poly-Si layer  $\approx 50$  nm) and  $J_0, \text{metal}, n^+ \approx 73.8$  fA/cm<sup>2</sup> (n<sup>++</sup>-poly-Si layer  $\approx 110$  nm), and the efficiency was improved by 0.12% owing to the increase in  $J_{sc}$  value of 0.28 mA/cm<sup>2</sup>. After optimizing the passivation process, the industrial-grade TOPCon bifacial cells reached an efficiency ( $\eta_{ff}$ ),  $V_{oc}$ ,  $J_{sc}$ , and FF values as high as 25.4%, 721 mV, 42.2 mA/cm<sup>2</sup>, and 83.5%, respectively.

## 1. Introduction

Tunnel oxide passivated contact technology has attracted a lot of attention from researchers working in the areas of solar cells in recent years. Due to the potential for high theoretical limit efficiency as high as 28.7% and low cost [1], TOPCon solar cells have become one of the prospective technologies in the photovoltaic (PV) market [2]. At present, the highest efficiency for n-TOPCon has achieved 26.4% on an area of 330.15 cm<sup>2</sup> at JinkoSolar [3]. The TOPCon structure consists of an ultrathin silicon oxide (SiO<sub>x</sub>) film and an n(+) doped polysilicon

(poly-Si) layer, which uses the concept of tunnel selectivity engineering. By employing thin SiO<sub>x</sub> layer, it was possible to obtain the tunneling selectivity which allows electron transmission from Si to n<sup>+</sup>-poly-Si layer while holes are repelled. The ideal thickness of tunnel oxide (1–2 nm) is advantage for capturing the photo-generated current of the solar cell. This structure can provide low recombination current density ( $J_0$ ) and low contact resistivity ( $\rho_c$ ) simultaneously. Römer et al. [4] reported that the lowest  $J_0$  was achieved to 0.66 fA/cm<sup>2</sup> for n<sup>+</sup> doped poly-Si/SiO<sub>x</sub> contact and 4.4 fA/cm<sup>2</sup> for p<sup>+</sup> doped poly-Si/SiO<sub>x</sub> contact. It is worth noting that  $J_0$  of p<sup>+</sup>-poly-Si layer is nearly 9 times higher than that

\* Corresponding author. Institute of Technology for Carbon Neutralization, Yangzhou University, School of Mechanical Engineering, Yangzhou, 225009, PR China.

\*\* Corresponding author.

E-mail addresses: [wangqinqin@yzu.edu.cn](mailto:wangqinqin@yzu.edu.cn) (Q. Wang), [dingjn@yzu.edu.cn](mailto:dingjn@yzu.edu.cn) (J. Ding).

of  $n^+$ -poly-Si layer, which is mainly attributed to a large difference of the diffusion characteristics of phosphorus and boron. On the one hand, it is different from the diffusivity of phosphorus and boron in poly-Si,  $\text{SiO}_x$  layer and c-Si wafer [5]. On the other hand,  $\text{SiO}_x$  layer can effectively inhibit the diffusion of phosphorus resulting in the formation of shallow doping profiles while boron readily diffuses into  $\text{SiO}_x$  layer leading to an increase in fixed oxide charges and interface trapped charge density, which further results in obtaining high  $J_0$  and  $\rho_c$  values [6,7]. Many efforts and processes have resolved these problems, such as optimizing process parameters [8,9] and boron-doped silicon paste [10].

Selective emitter (SE) technology is an industry-relevant promising strategy which features a lightly doped emitter in the passivated region and a heavily doped emitter underneath the metal fingers, which of high doping concentration and deep depth can effectively reduce interfacial recombination losses and the contact resistance [10]. Typically, the local-area doping method can be achieved by various technologies, such as wet chemical etch-back [11], ion implantation [12], laser doping [13], screen printing of boron and phosphorus-containing pastes [14], inkjet printing of doping sources [15,16] and thermal diffusions [17]. However, most of these mentioned technologies have some risks in the manufacturing solar cell process due to the dopant diffusion, the damage to the Si surface and over-alignment losses in the alignment with the front electrode during the printing process [18]. Additional masking and etching processes need to prevent these problems and to control the doping profiles. In this work, the selective emitter is formed by 3D printing mask technology, which could avoid the surface damage caused by other methods such as laser-assisted doping.

The fabrication of poly-Si films can be categorized into two main approaches—chemical vapour deposition (CVD) including plasma enhanced CVD (PECVD) [19,20], low pressure CVD (LPCVD) [21,22], atmospheric pressure CVD (APCVD) [23] and hot wire CVD (HWCVD) [24] and physical vapour deposition (PVD) including sputtering [25,26] or electron beam evaporation [27]. The  $\text{SiO}_x$  layer can be grown by chemical oxidation [28], ozone oxidation [29] and PECVD [30]. LPCVD has been the primary technology for manufacturing industrial TOPCon cells because of its high throughput and simple process [31,32]. Up to now, most of the thickness values of poly-Si layers are over 70 nm [33]. To further improve the cell performance, the suitable ultra-thin doped poly-Si needs to be developed. Usually, a high thermal annealing step is used to crystallize a-Si layer into a doped poly-Si layer, and dopants from poly-Si layers can diffuse extensively into the c-Si and compromise the passivation quality during this process [34]. Therefore, how to balance the thickness of poly-Si layer and dopant diffusion remains as one of the challenging and critical tasks.

After reviewing the previous publications [21,22,30–32], the effect of  $\text{SiO}_x/n^+$ -poly-Si process parameters on the n-TOPCon solar cells has not yet been thoroughly and deeply studied. Therefore, this study focuses on the  $\text{SiO}_x/n^+$ -poly-Si process of n-TOPCon solar cells, which consisted of screen-printed metallic contacts on both sides fabricated from 182 mm  $\times$  182 mm  $\times$  0.14 mm Cz-Si wafers through an industrial-type process with the fixed Ag/Al and Ag pastes. To this end, the  $\text{SiO}_x/n^+$ -poly-Si process parameters with respect to their influences on the ECV profiles,  $J_0$  and  $\rho_c$  were investigated. After optimizing the process, we simulated selective  $n^+$ -poly-Si based passivating contacts (abbreviated as Poly-SE) formed by the 3D printing mask technology and secondary LPCVD/phosphorus diffusion and investigated their passivation performance, photoelectronic performance and the  $I$ - $V$  parameters of solar cells, i.e., efficiency ( $\eta_{ff}$ ), open-circuit voltage ( $V_{oc}$ ), fill factor (FF), series resistance ( $R_{ser}$ ) and short-circuit current density ( $J_{sc}$ ).

## 2. Experimental methods

### 2.1. Solar cell fabrication

We manufactured the n-TOPCon cells from commercially available 182 mm  $\times$  182 mm n-type Cz-Si wafers with resistivity of 0.5–2  $\Omega$  cm

and thickness of  $140 \pm 10$   $\mu\text{m}$ . The wafers were textured in an alkaline (KOH) solution and subsequently cleansed in a solution of HF. The front Boron (B)-selective emitters ( $R_{\square,p++} = 75$   $\Omega/\text{sq}$ ,  $R_{\square,p+} = 230$   $\Omega/\text{sq}$ ) were formed in a quartz tube furnace containing  $\text{BCl}_3$  gas using LYDOP™ system (Laplace) and Laser doping technology with the width of 90–100  $\mu\text{m}$  (DR laser, 532 nm,  $>20\text{MKHz}$ ). After B diffusion, the rear side was polished by a mixed solution of HF and  $\text{HNO}_3$ . Due to the boron silicate glass layer formed during the boron doping step, this layer acts as a polishing mask layer to protect the front structure during the polishing process. The rear side stack, which consists of a  $\text{SiO}_x$  ( $1.6 \pm 0.2$  nm) layer and an intrinsic a-Si ( $140 \pm 20$  nm) layer, was formed by low-pressure chemical vapour deposition (LPCVD). The as-prepared samples were then annealed in a tube furnace at 880  $^\circ\text{C}$  for 45 min using a mixture gas of  $\text{POCl}_3$ ,  $\text{O}_2$ , and  $\text{N}_2$  to crystallize the a-Si to form poly-Si and simultaneously doped with phosphorus. Then, phosphorous silicate glass (PSG) was removed by etching in diluted HF solution, and the doping profiles of the  $\text{SiO}_x/n^+$ -poly-Si layers were tested by electrochemical capacitance voltage (ECV) profiling. The  $J_0$  of  $\text{SiO}_x/n^+$ -poly-Si layers under different process conditions was measured by two-side passivation of  $\text{SiN}_x$  using a Sinton WCT-120 system (Boulder, CO, USA). The thickness of  $\text{SiN}_x$  was 75 nm. Similar samples with acid-etched surface were screen-printed with Ag contact lines on only one side, with nine different pitches as the  $J_0$ , metal test. The Ag paste was then exposed to fire in an industrial belt-firing furnace at a peak firing temperature of  $735 \pm 5$   $^\circ\text{C}$  with the finger side facing up. The  $J_0$ , metal values for the different metallization fractions  $f$  were calculated by the Weixin PL system (VS-6841A-210). Meanwhile, the contact resistivity ( $\rho_c$ ) was obtained from the H patterns (16 busbar (BB) - 142 fingers) printed on one side of the  $J_0$  sample of 0.8–1  $\Omega$  cm n-type Cz-Si wafers. Fig. S1 shows the principle diagram of transfer-length-method. In this study, we investigated two key process parameters for the  $\text{SiO}_x$  layers (see Table 1 (i)), and three key process parameters for the phosphorus-diffused poly-Si contacts, respectively (see Table 1(ii)).

The  $\text{SiO}_x/n^{++}$ -poly-Si and  $\text{SiO}_x/n^+$ -poly-Si layers of the selective poly-Si based passivating contacts on n-TOPCon with B-selective emitters, as shown in Fig. 1, were fabricated by 3D printing and secondary LPCVD/phosphorus diffusion respectively, and the cell fabrication sequence is displayed in Table 2. After acid-etched process, the rear  $\text{SiO}_x/n^{++}$ -poly-Si layer was formed in LPCVD and a high-temperature quartz tube furnace containing  $\text{POCl}_3$  gas. The 3D printing mask technology was placed on the metal contact area and then removed after removing the PSG and  $\text{SiO}_x/n^{++}$ -poly-Si layer in the non-mask area. Among them, the  $\text{SiO}_x/n^{++}$ -poly-Si layer was removed by a polishing process (KOH/polishing additives) in the non-mask area, whereas the PSG in the contact area acts as an etch mask. The  $\text{SiO}_x/n^+$ -poly-Si layer was also prepared in LPCVD with a high-temperature quartz tube furnace containing  $\text{POCl}_3$  gas. After again cleaning the wafers again and removing boron silicate glass (BSG) and PSG, the poly-Si wraparound side was etched in inline treatment with HF and batch-type treatment with a mixed solution of KOH and polishing additives to obtain an  $\text{SiO}_x/n^+$ -poly-Si layer on only one side. Then, the front and rear passivation of the cell was carried out using 4 nm- $\text{AlO}_x$ /78 nm- $\text{SiN}_x$  and 75 nm- $\text{SiN}_x$ , respectively. The wafer was metallized by screen-printing and firing of a metal paste using an H-patterned grid design on both sides. Commercial Ag/Al and Ag pastes were used as the finger of front and the rear metal grids, respectively. A 16-BB configuration was used for both the front and rear sides with floating busbar contact paste. The cells were then manufactured by fast firing in a conveyor belt furnace at a peak firing temperature of  $735 \pm 5$   $^\circ\text{C}$ .

### 2.2. Characterization

The current-voltage ( $I$ - $V$ ) parameters were measured using a Wavelabs tester. The implied  $V_{oc}$  ( $iV_{oc}$ ) values of the control samples were determined using a Sinton WCT-120 lifetime tester under 1-sun illumination. The  $J_0$  values of the samples were measured using WCT-

**Table 1**Process conditions and main results of (i) SiO<sub>x</sub> layers, (ii) n<sup>+</sup>-doped poly-Si layers and (iii) a-Si layers.

Items	Conditions	SiO <sub>x</sub> Layers formation process		a-Si Layers formation process				n <sup>+</sup> -doped poly-Si layers formation process				Main results								
		<i>t</i> <sub>oxidation</sub> (min)	<i>t</i> <sub>pressure</sub> (min)	<i>T</i> (°C)	<i>T</i> (min)	<i>G</i> <sub>SiH4</sub> (sccm)	ECV (nm)	<i>T</i> <sub>deposition</sub> (°C)	<i>G</i> <sub>POCl3</sub> (sccm)	<i>T</i> <sub>drive in</sub> (°C)	<i>R</i> <sub>□</sub> (Ω/sq)	<i>ρ</i> <sub>c</sub> (mΩ. cm <sup>2</sup> )	<i>Lifetime</i> (μs)	<i>J</i> <sub>0</sub> (fA/ cm <sup>2</sup> )	<i>iV</i> <sub>oc</sub> (mV)	Investigation				
(i) : Influence of process parameters on the SiO <sub>x</sub> layer	Condition 1	5	5	600	44	500	125	790	1800	900	50.1	1.4	3160	5.2	736	The distribution number of O and Si <sup>4+</sup> content which is a key indicator of the quality of SiOx layer				
			10								52.4	2.5	2844	5.8	734					
			20								49.8	4.2	2246	7.7	729					
	Condition 2	10	5								50.7	1.8	2864	5.6	734					
			10								48.8	2.9	3118	5.6	735					
			20								48.9	4.1	2110	7.8	729					
	Condition 3	5	10								52.4	2.5	2844	5.8	734					
											48.8	2.9	3078	5.6	735					
											50.7	3.5	2514	6.9	732					
											51.6	3.9	1678	11	722					
(ii) : Influence of process parameters on the n <sup>+</sup> -doped poly-Si layer	Conditon A	5	5	500	100	790	1200	900	82.6	2.2	–	6.5	–	<i>J</i> <sub>0</sub> is as follows: <i>T</i> <sub>drive-in</sub> > <i>G</i> <sub>POCl3</sub> > <i>T</i> <sub>dep</sub> <i>ρ</i> <sub>c</sub> is as follows: <i>T</i> <sub>dep</sub> > <i>T</i> <sub>drive-in</sub> > <i>G</i> <sub>POCl3</sub>						
									1600	2.0	–	5.6	–							
									2000	1.7	–	7.7	–							
									2400	1.6	–	8.7	–							
	Conditon B		32		90	770	1800	900	92.7	3.8	–	5.6	–							
									67.8	1.7	–	5.7	–							
									44.2	1.2	–	6.6	–							
	Conditon C		43		120	790	1800	860	66.8	2.0	–	10.0	–							
									880	1.7	–	7.0	–							
									900	1.4	–	4.9	–							
									905	49.9	1.3	–	9.0	–						
(iii) : Influence of a-Si layer thickness	30 nm	5	5	600	15	500	30	790	Adjusti-ng P diffusi-on process	900	163.8	2.7	–	13.7	–	The influence of n <sup>+</sup> -poly-Si layer is about 0.0093 mA/cm <sup>2</sup> per nm.				
	50 nm														115.5		2.3	–	5.0	–
	70 nm														81.3		1.9	–	5.5	–
	90 nm														62.2		0.9	–	5.6	–
	110 nm														55.6		0.9	–	5.2	–

*t*<sub>oxidation</sub>: post-oxidation duration.*t*<sub>pressure</sub>: constant pressure duration.*G*<sub>SiH<sub>4</sub></sub>: SiH<sub>4</sub> gas flow rate.*T*<sub>deposition</sub>: deposition temperature.*G*<sub>POCl<sub>3</sub></sub>: POCl<sub>3</sub>-N<sub>2</sub> carrier gas flow rate.*T*<sub>drive-in</sub>: drive in temperature.*J*<sub>0</sub>: emitter dark saturation current density.*iV*<sub>oc</sub>: implied open circuit voltage.*J*<sub>0</sub>: emitter dark saturation current density.*ρ*<sub>c</sub>: the contact resistivity.

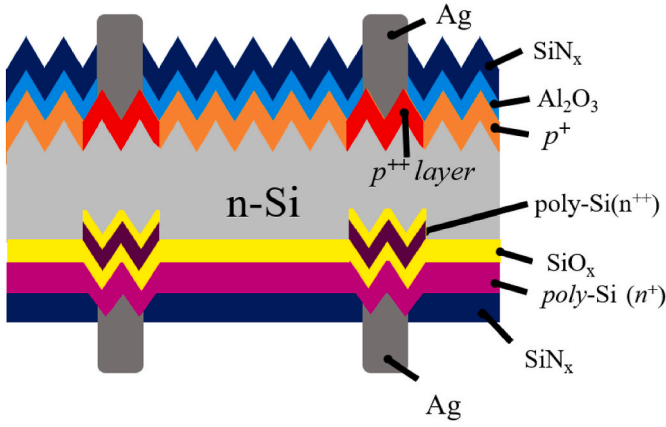


Fig. 1. n-TOPCon solar cell with selective poly-Si based passivating contacts.

Table 2

Preparation process of selective poly-Si based passivating contacts.

Processes
Alkaline texture
Front surface p <sup>+</sup> emitter
p <sup>++</sup> emitter (Laser doping)
Annealing
Rear etching
SiO <sub>x</sub> + i-Poly
n <sup>++</sup> doped poly-Si
3D printing mask technology
Clean 1 and polishing process
SiO <sub>x</sub> + i-Poly
n <sup>+</sup> doped poly-Si
Clean 2
AlO <sub>x</sub> /SiN <sub>x</sub> passivation
Screen printing and sintering

120 Sinton system and extracted at an excess carrier density of  $3 \times 10^{15} \text{ cm}^{-3}$  [34], and the  $J_{0, \text{metal}}$  values of the samples were calculated using the Weixin PL system (VS-6841A-210). The SiO<sub>x</sub>/n<sup>+</sup>-poly-Si profiles of the monitor wafers were measured using an ECV device (WEP CVP21) with an etchant of 0.1 M NH<sub>4</sub>F solution. The  $\rho_c$  of the screen-printed metallized contacts with different profiles was determined using the transfer-length method (TLM) (GP-4 TEST). The optical reflectance of the cell was measured using a PVE300-IVT instrument. During these tests, the optical losses were analyzed using the Current Loss Analysis Calculator V1.4 (the Solar Energy Research Institute of Singapore).

### 3. Results and discussion

#### 3.1. The effect of poly-Si based passivating contacts processes

##### 3.1.1. Influence of process parameters on the SiO<sub>x</sub> layer

The variables of the SiO<sub>x</sub> formation process parameters were the oxidation duration ( $t_{\text{oxidation}}$ )-the constant flow of O<sub>2</sub> fills the furnace tube for a certain time and the constant pressure duration ( $t_{\text{pressure}}$ )-under the atmospheric pressure (760000 mTorr) and the total O<sub>2</sub> source, the SiO<sub>x</sub> layer was deposited on the surface of Si for a certain time. Both influenced the SiO<sub>x</sub>/n<sup>+</sup>-poly-Si profiles, passivation performance ( $J_0$ ) and contact resistivity ( $\rho_c$ ) of n-TOPCon cells, analyzed using the LPCVD and POCl<sub>3</sub> tube furnace diffusion methods, and the results are shown in Table 1(i).

The ECV profiles for the SiO<sub>x</sub>/n<sup>+</sup>-poly-Si layer under different SiO<sub>x</sub> layer process conditions are shown in Fig. 2. In the first type, we varied the  $t_{\text{pressure}}$  under a constant  $t_{\text{oxidation}}$ : 1) Condition 1 [ $t_{\text{oxidation}} = 5 \text{ min}$  ( $t_{\text{pressure}} \approx 5/10/20 \text{ min}$ )] and Condition 2 [ $t_{\text{oxidation}} = 10 \text{ min}$  ( $t_{\text{pressure}} \approx 5/10/20 \text{ min}$ )] are shown in Figs. 2a and 2b. In the second type,  $t_{\text{oxidation}}$  was varied as the  $t_{\text{pressure}}$  was kept constant. Condition 3 [ $t_{\text{pressure}} = 10 \text{ min}$  ( $t_{\text{oxidation}} \approx 5/10/20/45 \text{ min}$ )] is shown in Fig. 2c. Generally, there was little variation in the surface concentration of the ECV profiles which was always larger than  $1 \times 10^{20} \text{ atoms/cm}^3$ , and the main difference was at “knee-shaped” profile where the concentration of the

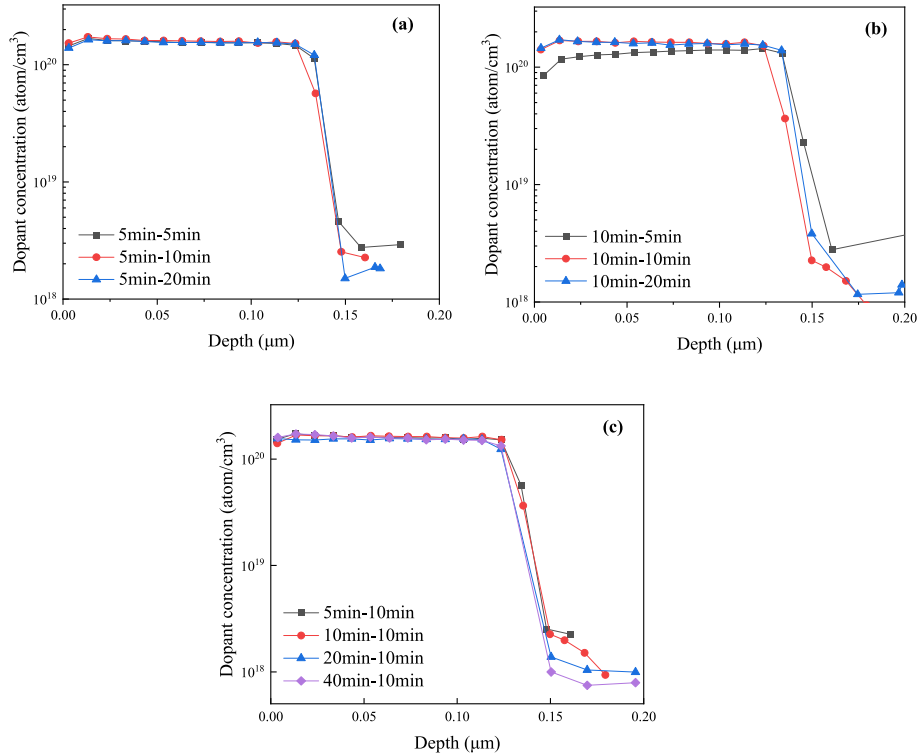


Fig. 2. ECV profiles of the change in the  $t_{\text{pressure}}$  under a constant  $t_{\text{oxidation}}$  (a) Condition 1 ( $t_{\text{oxidation}} = 5 \text{ min}$ ,  $t_{\text{pressure}} = 5/10/20 \text{ min}$ ), (b) Condition 2 ( $t_{\text{oxidation}} = 10 \text{ min}$ ,  $t_{\text{pressure}} = 5/10/20 \text{ min}$ ); the change in  $t_{\text{oxidation}}$  under the same  $t_{\text{pressure}}$  (c) Condition 3 ( $t_{\text{pressure}} = 10 \text{ min}$ ,  $t_{\text{oxidation}} = 5/10/20/40 \text{ min}$ ).

dopants in the poly-Si remained constant throughout the thickness of poly-Si and dropped just close to the poly-Si/SiO<sub>x</sub>/c-Si interface, and the “tail” of the dopant profile was defined as the part of the profile that diffused into the c-Si substrate from the surface concentration of  $1 \times 10^{20}$  atoms/cm<sup>3</sup> to  $1 \times 10^{19}$  atoms/cm<sup>3</sup>. Whenever  $t_{\text{oxidation}}$  and  $t_{\text{pressure}}$  were increased, the “knee-shaped” of the tail ECV profile became steeper. Because the thick oxide layer could prevent P from diffusing into Si with a steep tail ECV profile. Meantime, the quality of the SiO<sub>x</sub> layer can also influence P diffusion [36]. This result would be confirmed by the further experiment.

A comparison of SiO<sub>x</sub>/n<sup>+</sup>-poly-Si profiles measured by ECV with the corresponding SIMS profile reveals that the high amount of P dopants does not contribute to the electrical conductivity of the emitter (Fig. 3). The junction depth of SIMS profiles increases almost in equal proportion compared to ECV profile, about over 0.05 μm at a dopant concentration of  $N = 10^{19}$  atoms/cm<sup>3</sup>. It is inferred that a relatively large P atoms were diffused into Si, which will provide a poor passivation.

Fig. 4 shows the  $J_0$  values of the SiO<sub>x</sub>/n<sup>+</sup>-poly-Si layers under two different process parameters. In the case of  $t_{\text{pressure}}$ ,  $J_0$  increases from 5.2 to 7.8 fA/cm<sup>2</sup> with increasing the pressure duration from 5 to 20 min (Figs. 4a and 4b). This is consistent with the ECV profiles. For  $t_{\text{oxidation}}$ ,  $J_0$  increases from 5.6 to 6.9 fA/cm<sup>2</sup> as oxidation duration increases from 5 to 20 min (Fig. 4c), while the  $t_{\text{oxidation}} = 40$  min, the  $J_0$  had a high value of approximately 11 fA/cm<sup>2</sup>, which is more than 2 times than that of  $t_{\text{oxidation}} = 5$  min. From the above  $J_0$  data analysis compared with the conditions 2 and 3, it can be concluded that  $t_{\text{pressure}}$  and  $t_{\text{oxidation}}$  had a significant impact on  $J_0$  in the same total time of SiO<sub>x</sub> process owing to the distribution number of O and Si<sup>4+</sup> content on the growth of the SiO<sub>x</sub> layer. The data analysis of XPS spectra shows that the distribution number of O and Si<sup>4+</sup> content which is a key indicator of the quality of SiO<sub>x</sub> layer. The higher the SiO<sub>2</sub> content, the better the passivation quality (Fig. S2). And a thick SiO<sub>x</sub> layer was usually endowed with a relatively high passivation-quality but a poor tunneling selectivity, resulting in low FF. While the sheet resistance on p-type silicon of these three conditions has barely change, all of them are equal to around 50Ω/sq, it is indicated that under the same thickness of poly-Si layer, the thickness of SiO<sub>x</sub> layer does not determine the total doping concentration (Fig. S3).

The contact resistivity,  $\rho_c$ , for SiO<sub>x</sub>/n<sup>+</sup>-poly-Si layers with variations in the two key process parameters after sintering at  $735 \pm 5^\circ\text{C}$  is shown in Fig. 5. The confidence interval for the median of  $\rho_c$  is illustrated by the diamond-box plot. The  $\rho_c$  increased significantly from 1.4 to 1.8 mΩ cm<sup>2</sup>

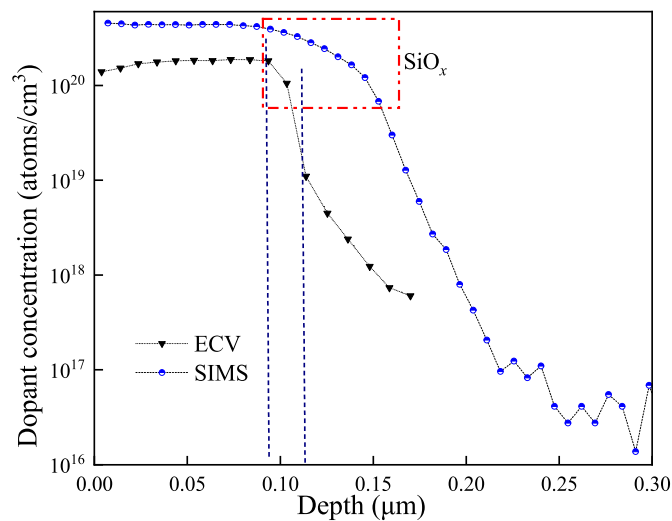


Fig. 3. The profiles of the SiO<sub>x</sub>/n<sup>+</sup>-poly-Si layer measured by ECV and SIMS, respectively (The dashed line: represents the gradual process of phosphorus concentration from the n<sup>+</sup>-poly-Si layer to the SiO<sub>x</sub> layer).

to 4.2 mΩ cm<sup>2</sup> by increasing the  $t_{\text{pressure}}$  from 5 to 20 min at  $t_{\text{oxidation}} = 5$  and 10 min, respectively (Figs. 5a and 5b). And for the varying  $t_{\text{oxidation}}$  process parameters,  $\rho_c$  can also be increased slightly from 2.5 to 3.9 mΩ cm<sup>2</sup> as oxidation duration increased from 5 to 40 min, as shown in Fig. 5c. Both  $t_{\text{pressure}}$  and  $t_{\text{oxidation}}$  had a significant influence on  $\rho_c$  which was mainly related to the thick oxide layer without good tunneling effect rather than sheet resistance, resulting in high contact resistivity. This is consistent with the “knee-shaped” of the tail ECV profile. In this study, the cells with a SiO<sub>x</sub> layer obtained under the 5 min  $t_{\text{oxidation}}$  -5 min  $t_{\text{pressure}}$  had a low  $J_0$  5.2 fA/cm<sup>2</sup> and low  $\rho_c$  1.4 mΩ cm<sup>2</sup>, which was attributed to the suitable thickness of the SiO<sub>x</sub> layer to effectively control the P dopants diffusing into Si. In the subsequent studies, the 5 min  $t_{\text{oxidation}}$  -5 min  $t_{\text{pressure}}$  were used as the optimal technological conditions for the growth of SiO<sub>x</sub> layer.

### 3.1.2. Influence of process parameters on the P doped poly-Si layer

In order to study the passivation properties of a-Si layer, we designed three groups of experiments, as shown in Table 3. One is SiO<sub>x</sub>/a-Si layer without any process (abbreviated as Poly-unannealed), the second is SiO<sub>x</sub>/a-Si layer after annealing without phosphorus doping (abbreviated as Poly-annealed), and the last is SiO<sub>x</sub>/a-Si layer after annealing with phosphorus doping (abbreviated as n<sup>+</sup>-poly-Si). All of them were passivated by SiN<sub>x</sub> layer and then tested for  $iV_{oc}$  before and after sintering.

The  $iV_{oc}$  values of the n-TOPCon cells were measured using the quasi steady-state photoconductivity (QSSPC) technique, and the results are shown in Fig. 6. Before sintering, the Poly-annealed and n<sup>+</sup>-poly-Si samples have the same high  $iV_{oc}$  of about 740 mV, while the Poly-unannealed sample has the lowest  $iV_{oc}$  of about 719.8 mV, as shown in Fig. 6a. For the annealing or phosphorus doping process, the H atoms from SiH<sub>4</sub> gas in SiO<sub>x</sub>/a-Si layer can be released to passivate the defect density. However, as shown in Fig. 6b, after sintering at  $735 \pm 5^\circ\text{C}$ , the order of change in  $iV_{oc}$  for sintering samples compared to unsintering samples is Poly-annealed (40 mV) > Poly-unannealed (15 mV) > n<sup>+</sup>-poly-Si (8 mV). This high decreased  $iV_{oc}$  of Poly-annealed samples are partly owing to in the poor stability at high temperature. However, after phosphorus doping process, n<sup>+</sup>-poly-Si sample has a small change in  $iV_{oc}$ , which is related to high temperature doping process fixing part of H atoms to escape. Through the above analysis, it finds why we choose the n<sup>+</sup>-poly-Si layer for the current high temperature process. However, how to control doping concentration of the as-prepared n<sup>+</sup>-poly-Si layer also needs to be considered. The influences of variables of the process parameters, including the POCl<sub>3</sub>-N<sub>2</sub> carrier gas flow rate at the deposition ( $G_{\text{POCl}_3}$ ), deposition temperature ( $T_{\text{dep}}$ ), drive in temperature ( $T_{\text{drive-in}}$ ) on the n<sup>+</sup>-poly-Si profiles,  $J_0$ ,  $\rho_c$  and optical reflection of n-TOPCon cells were analyzed using the POCl<sub>3</sub> tube furnace diffusion method.

The ECV profiles for the n<sup>+</sup>-poly-Si layer under different process conditions are shown in Fig. 7.  $G_{\text{POCl}_3}$  was set as 1200, 1600, 2000 and 2400 sccm using a single-variable process parameter, Fig. 7a shows the ECV profiles as a function of  $G_{\text{POCl}_3}$ .  $T_{\text{dep}}$  was set as 770, 790 and 810 °C, and the ECV profiles as a function of  $T_{\text{dep}}$  are shown in Fig. 7b.  $T_{\text{drive-in}}$  was set as 860, 880, 900 and 905 °C, and the ECV profiles as a function of  $T_{\text{drive-in}}$  are shown in Fig. 7c.

Generally, it can be found that the profiles were influenced much more by the process temperature than the POCl<sub>3</sub>-N<sub>2</sub> carrier gas flow.  $G_{\text{POCl}_3}$  was much less sensitive while the value was more than 1200 sccm (Fig. 7a). This was mainly because POCl<sub>3</sub> deposition at a relatively low temperature led to low phosphorus diffusivity. In particular,  $T_{\text{dep}}$  had a significant impact on the surface concentration of the profiles. With increasing  $T_{\text{dep}}$ , more dopants were diffused into the poly-Si layer as shown in Fig. 7b. With increasing  $T_{\text{drive-in}}$ , there is the almost same surface concentration, but it affects the “knee-shaped” of the tail ECV profile (Fig. 7c). For example, when  $T_{\text{drive-in}}$  achieved to 905 °C, there is a sharply drop and then a rise again, indicating that more phosphorus diffused into SiO<sub>x</sub> layer and decreased the passivation performance.

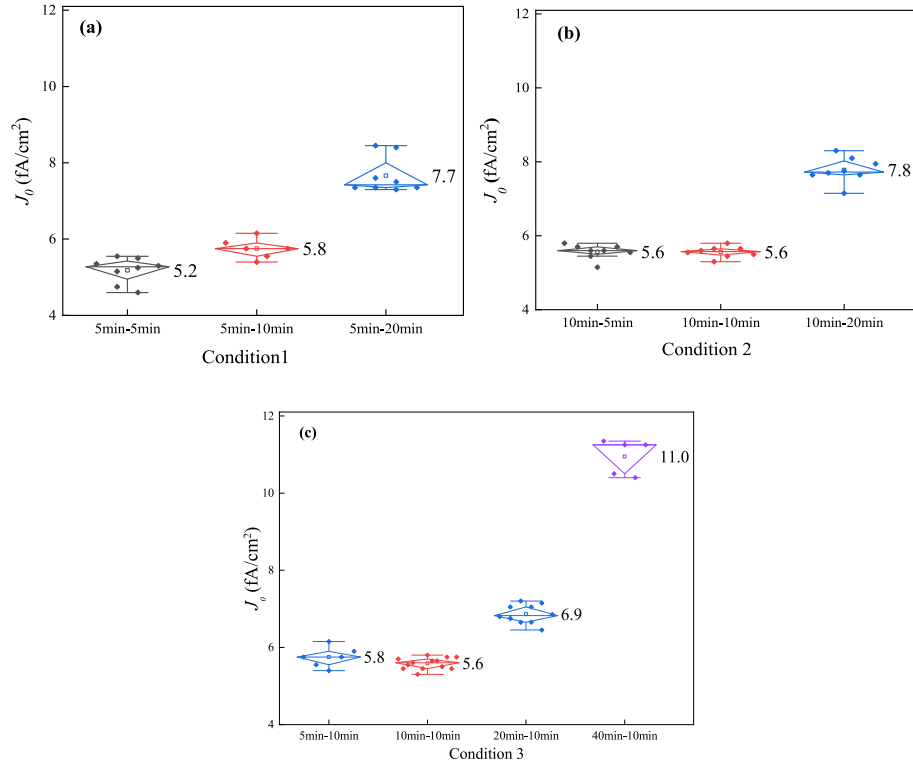


**Fig. 4.**  $J_0$  values in the passivated regions of (a) Condition 1 ( $t_{\text{oxidation}} = 5$  min,  $t_{\text{pressure}} = 5/10/20$  min), (b) Condition 2 ( $t_{\text{oxidation}} = 10$  min,  $t_{\text{pressure}} = 5/10/20$  min) and (c) Condition 3 ( $t_{\text{pressure}} = 10$  min,  $t_{\text{oxidation}} = 5/10/20/40$  min).

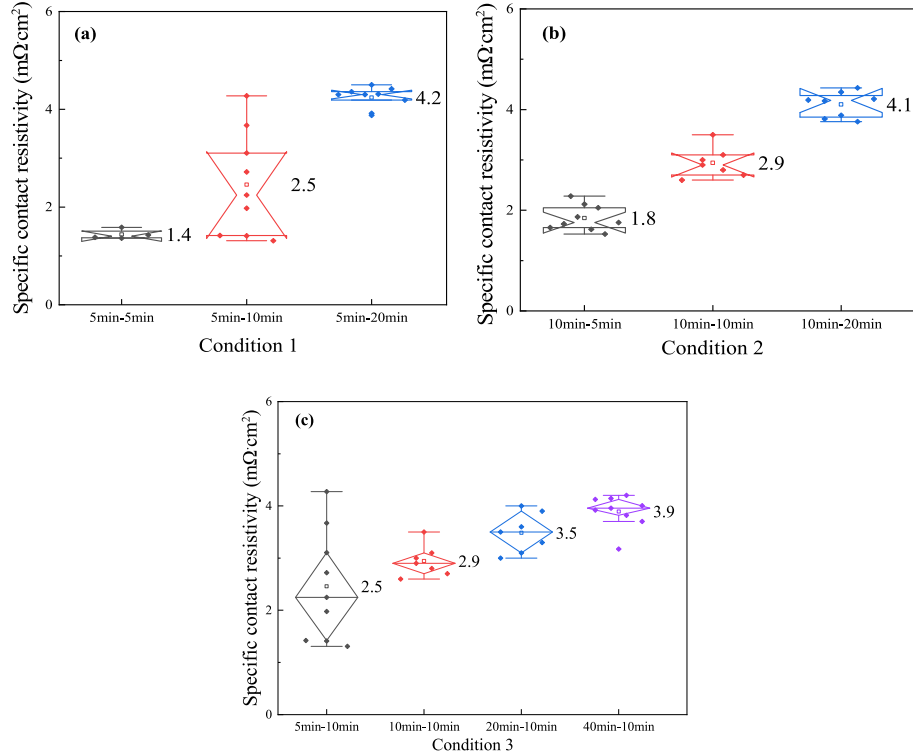


**Fig. 5.** Contact resistivity of (a) Condition 1 ( $t_{\text{oxidation}} = 5$  min,  $t_{\text{pressure}} = 5/10/20$  min), (b) Condition 2 ( $t_{\text{oxidation}} = 10$  min,  $t_{\text{pressure}} = 5/10/20$  min) and (c) Condition 3 ( $t_{\text{pressure}} = 10$  min,  $t_{\text{oxidation}} = 5/10/20/40$  min).

Fig. 8 shows the  $J_0$  values of the  $n^+$ -poly-Si layers under three different process parameters. In the case of  $G_{\text{POCl}_3}$ ,  $J_0$  increases from 5.6 to 8.7 fA/cm<sup>2</sup> with increasing POCl<sub>3</sub>-N<sub>2</sub> carrier gas flow from 1600 to

2400 sccm (Fig. 8a). However, when  $G_{\text{POCl}_3}$  drops to 1200 sccm, the  $J_0$  increases to 6.5 fA/cm<sup>2</sup>. Under the condition of  $G_{\text{POCl}_3} = 1200$  sccm, the flow rate of POCl<sub>3</sub> is lower compared to other conditions. As a result, the



**Table 3**Preparation of three groups of SiO<sub>x</sub>/a-Si layers samples.

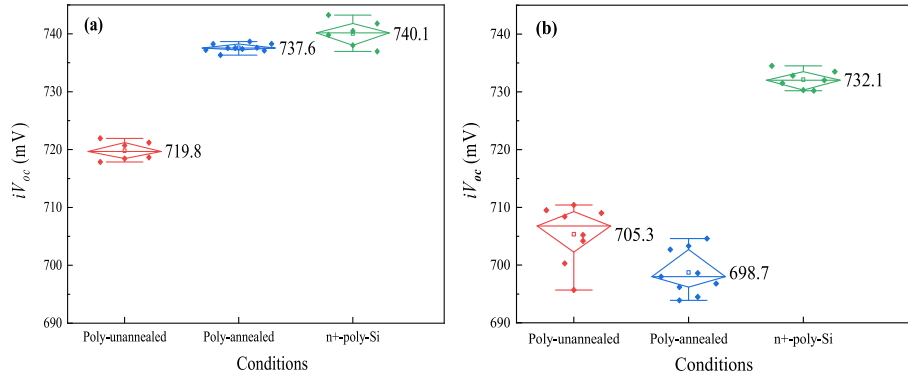
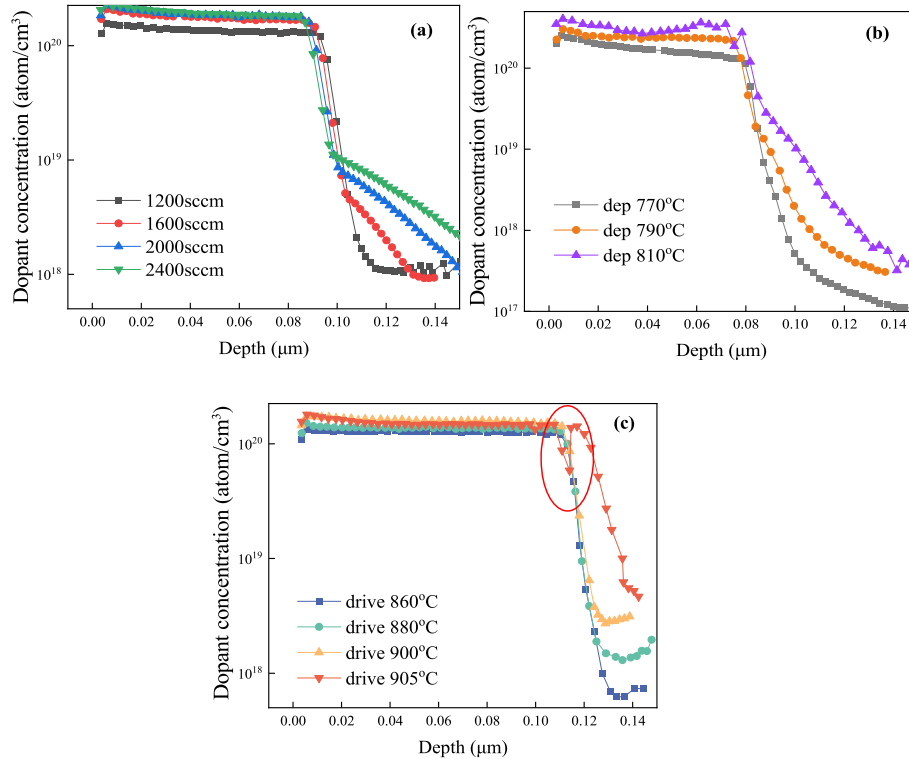
Process of SiO <sub>x</sub> /a-Si monitoring wafers		
2 Ω cm Silicon Wafers (N-type)		
Rough polishing		
Texturing		
Cleaning		
LPCVD deposition of SiO <sub>x</sub> /a-Si		
/	/	Phosphorus doping
/	Annealing	Annealing
Double-sided deposition of SiN <sub>x</sub>		
Poly-unannealed	Poly-annealed	n <sup>+</sup> -poly-Si

concentration of Phosphorus-dopants on the surface is low, leading to a reduced number of Phosphorus-dopants diffusing into the surface. Consequently, there is insufficient energy band bending occurring into the surface, which results in the poor field effect passivation. For  $T_{\text{dep}}$ ,  $J_0$  exhibits a small change of approximately 1 fA/cm<sup>2</sup> with increasing  $T_{\text{dep}}$  from 770 to 810 °C (Fig. 8b). For  $T_{\text{drive in}}$ ,  $J_0$  shows a slight decrease from

10 to 4.9 fA/cm<sup>2</sup> as  $T_{\text{drive in}}$  increases from 860 to 900 °C (Fig. 8c), while the  $T_{\text{drive in}}$  achieved to 905 °C, the  $J_0$  increased to 9 fA/cm<sup>2</sup>, which is consistent with the ECV profiles, which is owing to destroying the quality of SiO<sub>x</sub> layer and leading to the poor passivation. From the above  $J_0$  data analysis, it can be concluded that the drive-in temperature had the greatest impact on  $J_0$ , followed by the POCl<sub>3</sub>-N<sub>2</sub> carrier gas flow rate at the deposition, which is mainly related to the chemical passivation of SiO<sub>x</sub> layer induced by P-indiffusion into Si at high temperature and the field effect passivation induced by doping concentration.

Fig. S4 shows the  $R_{\square}$  of the n<sup>+</sup>-poly-Si layers under p-type silicon with variations of the three key process parameters. The surface concentration of n<sup>+</sup>-poly-Si layer is high, the sheet resistance is low, which is mainly owing to total doping level. When the  $G_{\text{POCl}_3} \approx 2000$  sccm and the  $T_{\text{drive in}} \approx 900$  °C were applied, the changes of  $R_{\square}$  have been balanced.

The  $\rho_c$  for n<sup>+</sup>-poly-Si layers with variations in the three key process parameters is shown in Fig. 9. The  $\rho_c$  decreased from 2.2 to 1.6 mΩ·cm<sup>2</sup> by increasing  $G_{\text{POCl}_3}$  from 1200 to 2400 sccm (Fig. 9a). And in the case of  $T_{\text{dep}}$ , the  $\rho_c$  decreased from 3.8 to 1.2 mΩ·cm<sup>2</sup> by increasing  $T_{\text{dep}}$  from

**Fig. 6.** Average  $iV_{oc}$  of three groups SiO<sub>x</sub>/a-Si layer of experimental samples (a) before; (b) after sintering.**Fig. 7.** ECV profiles of n<sup>+</sup>-poly-Si layers with variations of the three key process parameters:  $G_{\text{POCl}_3}$  (a),  $T_{\text{dep}}$  (b),  $T_{\text{drive-in}}$  (c).

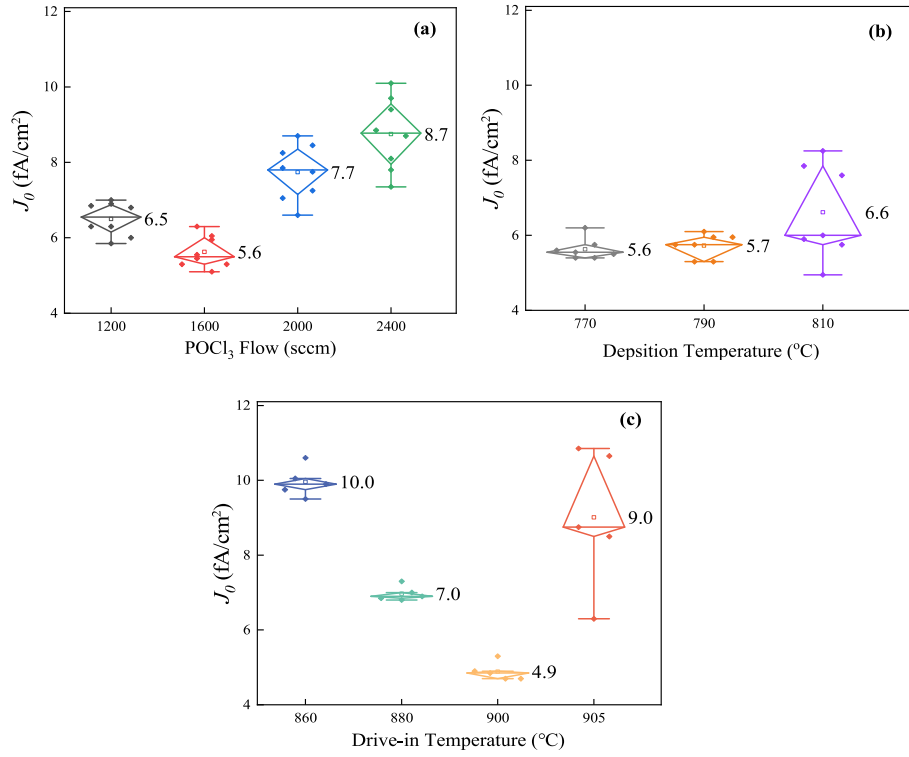


**Fig. 8.**  $J_0$  values of  $n^+$ -poly-Si layers with variations of the three key process parameters:  $G_{\text{POCl}_3}$  (a),  $T_{\text{dep}}$  (b),  $T_{\text{drive-in}}$  (c).

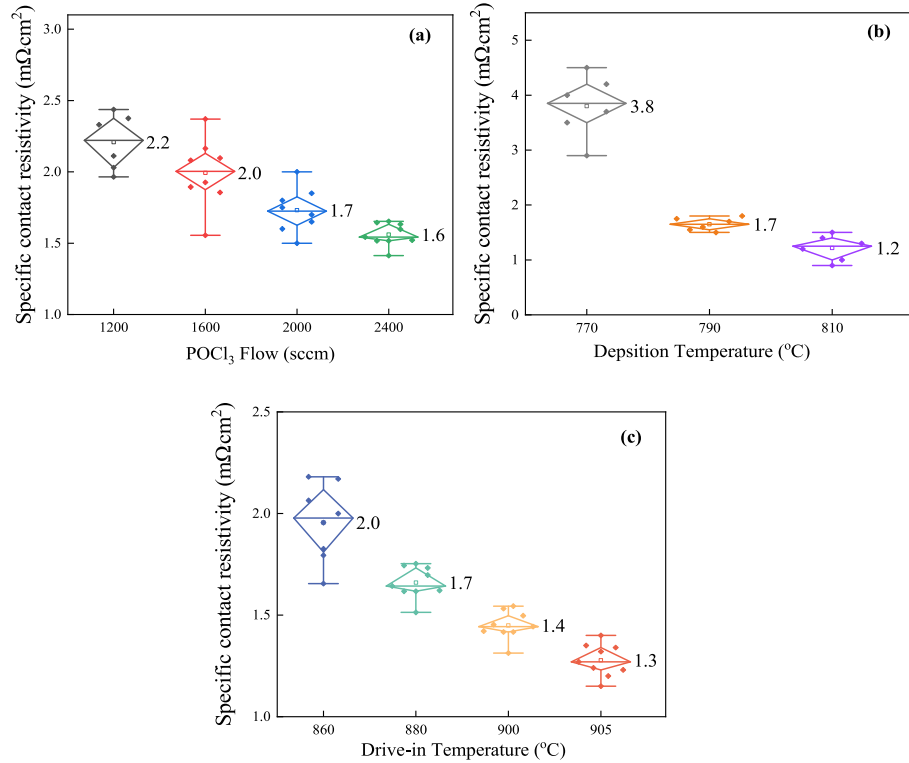


**Fig. 9.** Contact resistivity of  $n^+$ -poly-Si layers with variations of the three key process parameters:  $G_{\text{POCl}_3}$  (a),  $T_{\text{dep}}$  (b),  $T_{\text{drive-in}}$  (c).

770 to 810 °C (Fig. 9b). For the change of  $T_{\text{drive-in}}$  process parameter, the  $\rho_c$  also decreased significantly from 2.0 to 1.3 mΩ cm<sup>2</sup> as  $T_{\text{drive-in}}$  increased from 860 to 905 °C, as shown in Fig. 9c. For the three characteristics observed, the sequence of their impact on the  $\rho_c$  is as follows:  $T_{\text{dep}} > T_{\text{drive-in}} > G_{\text{POCl}_3}$ . From the above  $\rho_c$  analysis, the influence of the

contact resistivity is still related to the total doping level, which is consistent with the ECV profiles. The flow rate of  $\text{POCl}_3$  had the least influence on the P-doping profile and  $\rho_c$ , it is mainly because the temperature determines the solid solubility of phosphorus.

The reflectance profiles with different  $\text{POCl}_3$ - $\text{N}_2$  carrier gas flow rates



at the deposition are shown in Fig. 10, the etched surface without  $n^+$ -poly-Si layer has only one peak at wavelength of about 400 nm, and the reflectance ( $R$ ) reaches to 45%. However, the samples with  $n^+$ -poly-Si layer contain two peaks at wavelengths of 450 and 550 nm, and the  $R$  value is smaller than that of the etched surface at wavelengths of 450–800 nm. From the above analysis, the poly-Si layer is unsuited to be deposited in the front of solar cell due to much more parasitic absorption loss. Maybe it is because that the proportion of a-Si in poly-Si would retain approximate 20% after a high-temperature annealing process and the absorption coefficient of a-Si:H is higher than that of poly-Si in the wavelength of 400–700 nm for intensive photon energy leading to a high parasitic absorption loss [23,37]. On the contrary, it is suitable for the rear of solar cell. The  $R$  increased by decreasing  $G_{POCl_3}$  from 2400 to 1200 sccm, which has a high free carrier absorption (FCA) loss probably due to high doping, it is consistent with ECV profiles (Fig. 7a). From the above  $n^+$ -poly-Si layers data analysis, it can be concluded that the low doping concentration would lead to low FCA loss. A balance between the  $J_{sc}$  and FF is to find an appropriate doping concentration of  $n^+$ -poly-Si layer.

### 3.2. Selective poly-Si based passivating contacts

#### 3.2.1. Preparation and simulation

To select an appropriate  $n^+$ -poly-Si layers diffusion process, we fabricated five types of  $n^+$ -poly-Si layers on the polished surface by the change of the LPCVD deposition time and diffusion process parameters (Table 1(iii)). The ECV profiles, sheet resistance,  $J_0$ ,  $\rho_c$ , and near-infrared (NIR) parasitic absorbance current loss analysis of the  $n^+$ -poly-Si layers are shown in Fig. 11. Generally, as shown in Fig. 11a, all of  $n^+$ -poly-Si layers have nearly the same surface concentration of more than  $1 \times 10^{20}$  atoms/cm<sup>3</sup> and almost the same “knee-shaped” of the tail ECV profile with the thickness of  $n^+$ -poly-Si layers, which were annealed at the same high temperature with adjusting P diffusion process. While the sheet resistance on p-type silicon was increased from 56 to 164  $\Omega$ /sq with decreasing the thickness of  $n^+$ -poly-Si layers from 110 to 30 nm (Fig. 11b). The values of  $n^+$ -poly-Si layers exhibit a minor change of approximately 0.5 fA/cm<sup>2</sup> with the thickness from 50 to 110 nm, while the thickness of 30 nm has a high  $J_0$  value of >13 fA/cm<sup>2</sup> which indicates that the thickness of <50 nm cannot provide an effective field effect passivation (Fig. 11c). However, the  $\rho_c$  has a remarkable change, which decreased from 2.7 to 0.9 m $\Omega$ -cm<sup>2</sup> by increasing the thickness from 30 nm to 110 nm owing to the total doping concentration (Fig. 11d). Subsequently, the NIR parasitic absorbance current loss

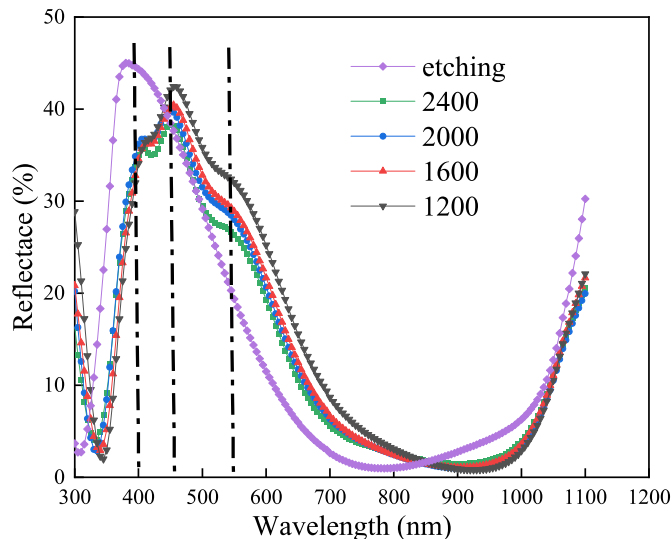


Fig. 10. Reflectance of the  $n^+$ -poly-Si layers on the etched surface with different  $POCl_3$  flows.

density was analyzed by Current Loss Analysis Calculator V1.4 software (Solar Energy Research Institute of Singapore), and the linear variation of NIR parasitic absorbance current loss density with the  $n^+$ -poly-Si layer thickness for all samples is shown in Fig. 11e. The slope of the current loss density against the thickness of  $n^+$ -poly-Si layer is equal to NIR parasitic absorbance current loss density per nanometer, which is thought to be related to the thickness of  $n^+$ -poly-Si layer about 0.0093 mA/cm<sup>2</sup> per nm. In a word, the  $n^+$ -poly-Si layers need to satisfy high-quality passivation and low parasitic absorption. While the  $n^+$ -poly-Si layers need to satisfy the conditions of corroded depth and  $\rho_c$  of the Ag paste, so the above analysis is proposed to assume 110 nm as  $n^+$ -poly-Si layer. The photograph of screen-printing pattern of the  $n^+$ -poly-Si layer sample with different metallization fractions is shown in Fig. 12a and the values of  $J_{0,metal,n++} \approx 73.8$  fA/cm<sup>2</sup> are displayed in Fig. 12b based on a simple linear interpolation of the measured data points calculated by the previous research method [35].

We simulated one batch of BKM (best known method, 110 nm) solar cells and Poly-SEs with different  $n^+$ -poly-Si layers on  $n^+$ -poly-Si layer (110 nm) using Griddler 2.5, and the total saturation current density in the cell ( $J_{0,total}$ ) and the  $J_0$  on the rear non-metallized area ( $J_{0,passivated\ area\ (rear)}$ ) was calculated using the measured values of  $J_0$  and  $J_{0,metal}$  according to Eq. (1) and (2), respectively. And the  $J_{sc}$  value was estimated on the reference value of 41.63 mA/cm<sup>2</sup> which is obtained by calculating the metal shielding area through Griddler 2.5 simulation, and NIR parasitic absorbance current loss density of  $n^+$ -poly-Si layer according to Eq. (3). The saturation current density of the bulk material ( $J_{0,bulk}$ ) was estimated to be 5 fA/cm<sup>2</sup>. The cell  $V_{oc}$  and FF values were calculated from  $J_{0,total}$  and  $\rho_c$  using an ideal one-diode model, the data related to B-SE simulation came from the previous studies [7] and the cell efficiency values were calculated by formula  $E_{ff} = V_{oc} \times J_{sc} \times FF$ , the results are shown in Table 4. The Poly-SE with a  $n^+$ -poly-Si layer of 50 nm had a higher  $E_{ff}$  of approximately 24.58%, thus obtaining a gain of 0.18% compared to BKM (110 nm), mainly owing to the increase  $J_{sc}$  of 0.49 mA/cm<sup>2</sup> and a slight advantage of  $J_{0,total}$ . We could not obtain a high FF, mainly because of the high lateral resistance of the  $n^+$ -poly-Si layer.

$$J_{0,total} = \{[(J_{0,metal} \times f_j) + (J_{0,p+} \times (1-f_{jmask})) + (J_{0,p++} \times (f_{jmask}-f_j)) \text{ (front)} + [(J_{0,metal} \times f_r) + (J_{0,n+} \times (1-f_{rmask})) + (J_{0,n++} \times (f_{rmask}-f_r)) \text{ (rear)}] + J_{0,bulk}\} \quad (1)$$

$$J_{0,passivated\ area\ (rear)} = (1-f_{rmask}) \times J_{0,n++} + (f_{rmask}-f_r) \times J_{0,n+} \quad (2)$$

$$J_{sc} = 41.63 + (Th_{-BKM} - Th_{-n+}) \times (1-f_{rmask}) \times 0.0093 \quad (3)$$

According to the simulation results, we fabricated a Poly-SE solar cell ( $n^+/n^+$  layer, 50/110 nm) and normal cells (BKM, 110 nm) based on the best simulation conditions, as shown in Table 4. The mask line of the  $n^+$ -poly-Si layer was relatively uniform with the 3D printing mask, the width of the mask line decreased from 180 to 150  $\mu$ m after polishing and RCA washing, and the mask line became smooth and clear, as shown in Fig. 13. The surface concentrations of the  $n^+$  and  $n^+$ -poly-Si layers were  $2.1 \times 10^{20}$  and  $1.85 \times 10^{20}$  atoms/cm<sup>3</sup> respectively, and the thickness values of the  $n^+$  and  $n^+$ -poly-Si layers were 50 and 110 nm, respectively (Fig. 11a), which provides a good photoelectronic performance for the lightly doped areas. The low  $J_{0,n+}$  and  $J_{0,metal,n++}$  values were measured to be 5 fA/cm<sup>2</sup> and 73.8 fA/cm<sup>2</sup>, respectively (Figs. 11c and 13b), which indicates the lightly and heavily doped areas exhibited a good passivation performance.

#### 3.2.2. Cell performance

The results of the  $iV_{oc}$  values and lifetime of the precursor structure are shown in Fig. S5. The Poly-SE solar cells did not show a good passivation performance, in which  $iV_{oc}$  decreased by only 1 mV compared with BKM, and the lifetime decreased by 17  $\mu$ s.

Table 5 lists the  $I$ - $V$  parameters of the BKM and Poly-SE solar cells. Poly-SE shows a higher  $J_{sc}$  of approximately 0.28 mA/cm<sup>2</sup> compared with BKM, which is attributed to the thin thickness of  $n^+$ -poly-Si layer.

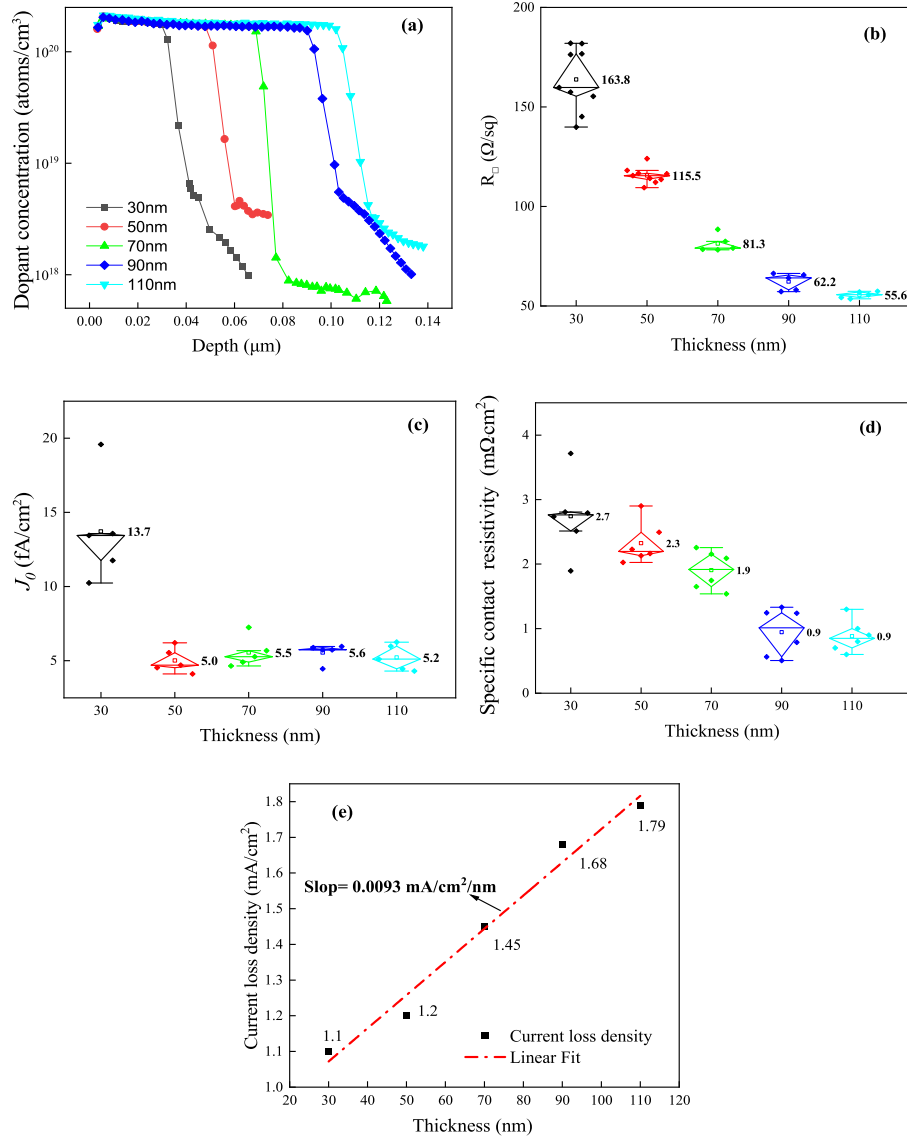


Fig. 11. ECV profiles (a), sheet resistance on p-type silicon (b),  $J_0$  (c),  $\rho_c$  (d) and NIR parasitic absorbance current loss density (e) of  $n^+$ -poly-Si layers.

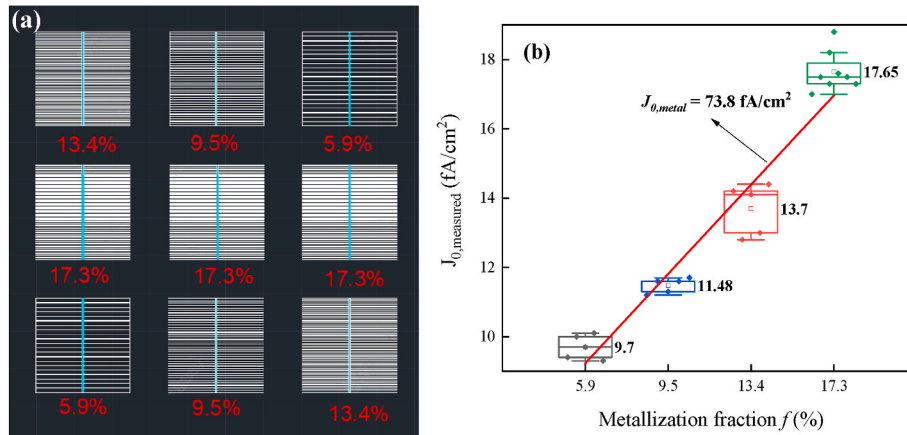


Fig. 12. The photograph of the screen-printing pattern of the samples with different metallization fractions from 5.9% to 17.3% (a) and  $J_{0,metal}$  (b) of  $n^+$ -poly-Si layer.

**Table 4**Detailed calculation of  $V_{oc}$ ,  $J_{sc}$  and FF using an ideal one-diode model.

Processes	BKM	Poly-SEs			
$n^{++}$ layer( $\Omega/sq$ )	56				
$n^{+}$ layer( $\Omega/sq$ )	56	164	116	81	62
$Th_{n^{++}}$ (nm)	110				
$Th_{n^{+}}$ (nm)	110	30	50	70	90
$J_{0e,metal}$ (rear fingers)[fA/cm <sup>2</sup> ]	73.8				
$J_{0,n^{++}}$ (rear)[fA/cm <sup>2</sup> ]	5.2				
$J_{0,n^{+}}$ (rear)[fA/cm <sup>2</sup> ]	5.2	13.7	5	5.5	5.6
$p^{++}$ layer( $\Omega/sq$ )	75				
$p^{+}$ layer( $\Omega/sq$ )	230				
$J_{0e,metal}$ (front fingers)[fA/cm <sup>2</sup> ]	412				
$J_{0,p^{++}}$ (front)[fA/cm <sup>2</sup> ]	25.8				
$J_{0,p^{+}}$ (front)[fA/cm <sup>2</sup> ]	9.9				
Metallized fraction (front ink fingers)( $f_{ink}$ )[%]	5.6%				
Metallized fraction (front fingers)( $f_f$ )[%]	1.7%				
Metallized fraction (rear fingers)( $f_r$ )[%]	2.7%				
Metallized fraction (rear ink fingers)( $f_{ink}$ )[%]	11.8%				
$J_{0,bulk}$ [fA/cm <sup>2</sup> ]	5				
$J_{0e,total}$ [fA/cm <sup>2</sup> ]	29.41	36.91	29.23	29.67	29.76
$\rho_c$ ( $p^{++}$ layer)[m $\Omega$ .cm <sup>2</sup> ]	1.30				
$\rho_c$ ( $n^{++}$ layer)[m $\Omega$ .cm <sup>2</sup> ]	0.90				
$V_{oc}$ (calculated)[mV]	713	708	713	713	713
FF[%]	82.22	81.3	81.9	82.1	82.2
$J_{sc}$ [mA/cm <sup>2</sup> ]	41.63	42.3	42.1	42.0	41.8
$E_{ff}$ [%]	24.40	24.35	24.58	24.55	24.49

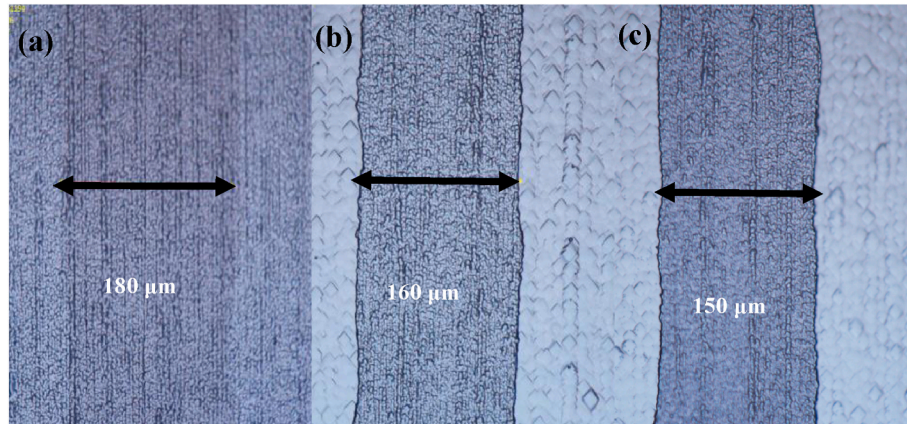
 $J_0$ : emitter dark saturation current density. $J_{0, metal}$ : the dark saturation current density at metal contact. $\rho_c$ : the contact resistivity.

However, there is a slightly fall for the  $V_{oc}$  of approximately 0.3 mV, which can be negligible. While  $R_s$  decreased, FF did not show any advantage, which may be owing to the influence of the high resistance of the  $n^{+}$ -poly-Si layer. However, in the best cell,  $R_s$  slightly increased, and FF also slightly increased which may be owing to the influence of the bulk time of Si wafer. The overall median efficiency increased by 0.12%. These results are basically consistent with the above simulation analysis, the only difference is the less gain of current density, which is mainly owing to the effect of manufacturing process of solar cells (RCA washing, the uniformity of sheet resistance and the line width/height of screen printing, etc.).

### 3.2.3. Failure analysis

To understand the effects of the Poly-SE solar cells, the current loss analysis was carried out using the Current Loss Analysis Calculator V1.4 software (based on the Yablonovitch limit of 46.43 mA/cm<sup>2</sup>) as shown in Fig. 14. Here, there are three primary advantages of Poly-SE from BKM, the one is "NIR parasitic absorption loss", the  $J_{sc}$  is increased by 0.59 mA/cm<sup>2</sup>, which is related to the rear polished surface and the thin thickness of the  $n^{+}$ -poly-Si layer. It is consistent with the result of simulation. The others are "blue loss" and "base collection loss", which get benefit from the additional RCA cleaning (Clean 1) and the gettering effect of P doping diffusion process. However, Poly-SE showed a disadvantage in terms of "ARC reflectance" and "Front surface escape", which is related to the polishing process leading to damage the front surface texture and to increase the reflectance. After process optimization, the  $J_{sc}$  value of Poly-SE can be further increased.

To improve the optical performance of n-TOPCon solar cells by simplifying the Poly-SE solar cell preparation process and optimizing the polishing process will be the future research direction.

**Fig. 13.** The photograph of the mask line of  $n^{++}$  layer after (a) mask, (b) polishing and (c) RCA cleaning.**Table 5**

I-V parameters of BKM and Poly-SE solar cells.

Conditions		$V_{oc}$ (mV)	$J_{sc}$ (mA/cm <sup>2</sup> )	$R_s$ m $\Omega$	FF (%)	$E_{ff}$ (%)	Cell area (cm <sup>2</sup> )
BKM	Median	718.0	40.78	0.0412	82.73	24.22	330.15
	Best cell	722.4	40.90	0.0414	82.86	24.48	
Poly-SE	Median	717.7	41.06	0.0407	82.65	24.34	
	Best cell	719.6	41.05	0.0417	82.95	24.50	

 $V_{oc}$ : open circuit voltage. $J_{sc}$ : short circuit current density. $R_s$ : series resistance.

FF: fill factor.

 $E_{ff}$ : efficiency.

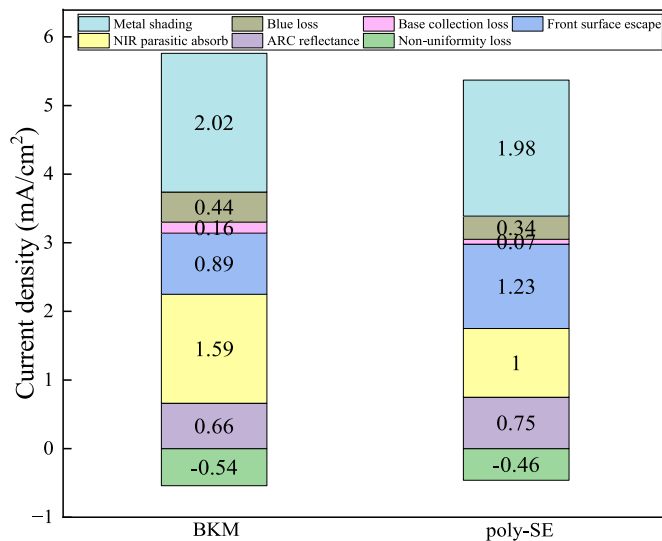


Fig. 14. Current loss analysis of BKM and Poly-SE cells.

#### 4. Conclusions

The influences of the  $\text{SiO}_x$  layer formation process parameters (the oxidation duration ( $t_{\text{oxidation}}$ ) and the constant pressure duration ( $t_{\text{pressure}}$ )), and the  $\text{POCl}_3$  tube diffusion process parameters (the  $\text{POCl}_3\text{-N}_2$  carrier gas flow rate at the deposition, deposition temperature, drive in temperature) on the  $\text{n}^+\text{-poly-Si}$  profiles,  $J_0$ ,  $\rho_c$  of n-TOPCon solar cells were studied. The  $t_{\text{oxidation}}$  and  $t_{\text{pressure}}$  had a significant impact on  $J_0$  and  $\rho_c$  values in the same total time of  $\text{SiO}_x$  process, which was mainly related to the distribution number of O and  $\text{Si}^{4+}$  content on the growth of the  $\text{SiO}_x$  layer. The drive-in temperature of P diffusion process had a stronger influence on  $J_0$  than the deposition temperature, which was mainly related to the chemical passivation of  $\text{SiO}_x$  layer induced by P-indiffusion into Si at high temperature.

Subsequently, we designed different thicknesses for the  $\text{n}^+\text{-poly-Si}$  layers. There was a significant positive correlation between  $\rho_c$  and sheet resistance and the thickness of  $\text{n}^+\text{-poly-Si}$  layer. The reduction in the thickness of poly-Si from 110 nm to 30 nm led to an increase in the short-circuit current density ( $J_{sc}$ ) per nanometer of  $\sim 0.0093 \text{ mA/cm}^2$  per nm, however,  $J_0$  values exhibited a minor change with the thickness from 50 to 110 nm. The analysis of high  $\rho_c$  and  $J_0$  values showed that for poly-Si layers with thickness of 30 nm, the paste might have spiked at the interface of  $\text{SiO}_x/\text{n}^+\text{-poly-Si}$ .

Based on the simulation results, we prepared Poly-SEs with  $J_0, \text{n}^+ \approx 5 \text{ fA/cm}^2$  ( $\text{n}^+\text{-poly-Si}$  layer  $\approx 50 \text{ nm}$ ) and  $J_0, \text{metal, n}^+ \approx 73.8 \text{ fA/cm}^2$  ( $\text{n}^+\text{-poly-Si}$  layer  $\approx 110 \text{ nm}$ ), using 3D printing mask technology and secondary LPCVD/phosphorus diffusion. There was an efficiency gain of 0.12% owing to the increase in  $J_{sc}$  value of  $0.28 \text{ mA/cm}^2$ , mainly owing to the thin thickness of  $\text{n}^+\text{-poly-Si}$  layer. The overall contribution of the Poly-SE to  $V_{oc}$  of the solar cells is negligible.

Through the optical loss analysis, the primary loss of Poly-SE from BKM was taken from ARC reflectance and Front surface escape, which was related to the polishing process leading to damaging the front surface texture and increasing the reflectance. After optimizing of the passivation process, the industrial-grade TOPCon bifacial cells reached an efficiency ( $\text{Eff}$ ),  $V_{oc}$ ,  $J_{sc}$ , and FF values as high as 25.4%, 721 mV,  $42.2 \text{ mA/cm}^2$ , and 83.5%, respectively.

#### CRediT authorship contribution statement

**Qinqin Wang:** Writing – review & editing, Writing – original draft, Supervision, Software, Resources, Methodology, Investigation, Formal analysis, Data curation. **Hui Peng:** Software, Methodology. **Siwen Gu:**

Formal analysis. **Kaiyuan Guo:** Resources. **Wangping Wu:** Writing – review & editing. **Bairu Li:** Writing – review & editing. **Lvzhou Li:** Writing – review & editing. **Ningyi Yuan:** Writing – review & editing. **Jianning Ding:** Writing – review & editing.

#### Declaration of competing interest

We declare that we do not have any commercial or associative interest that represents a conflict of interest in connection with the work submitted.

#### Data availability

Data will be made available on request.

#### Acknowledgements

This work has been partially supported by Jiangsu Province Cultivation base for State Key Laboratory of Photovoltaic Science and Technology (SKLPST 202201), the Natural Science Foundation of Jiangsu Province (Grants No. BE2022610, BE2022022-4), Jiangsu Province Engineering Research Center of High-Level Energy and Power Equipment (JSNYDL-202301).

#### Appendix A. Supplementary data

Supplementary data to this article can be found online at <https://doi.org/10.1016/j.solmat.2023.112458>.

#### References

- [1] J. Schmidt, R. Peibst, R. Brendel, Surface passivation of crystalline silicon solar cells: present and future, *Sol. Energy Mater. Sol. Cells* 187 (2018) 39–54, <https://doi.org/10.1016/j.solmat.2018.06.047>.
- [2] S.P. Padi, M.Q. Khokhar, S. Chowdhury, E.-C. Cho, J. Yi, Nanoscale  $\text{SiO}_x$  tunnel oxide deposition techniques and their Influence on cell parameters of TOPCon solar cells, *Trans. Electr. Electron. Mater.* 22 (2021) 557–566, <https://doi.org/10.1007/s42341-021-00356-7>.
- [3] .d. Jinko Solar (n. <https://www.jinkosolar.com/en/site/newsdetail/1827>. (Accessed 17 March 2023).
- [4] U. Romer, R. Peibst, T. Ohrdes, B. Lim, J. Krugener, T. Wietler, R. Brendel, Ion implantation for poly-Si passivated back-junction back-contacted solar cells, *IEEE J. Photovoltaics* 5 (2015) 507–514, <https://doi.org/10.1109/JPHOTOV.2014.2382975>.
- [5] F. Feldmann, J. Schön, J. Niess, W. Lerch, M. Hermle, Studying dopant diffusion from Poly-Si passivating contacts, *Sol. Energy Mater. Sol. Cells* 200 (2019), 109978, <https://doi.org/10.1016/j.solmat.2019.109978>.
- [6] H. Wei, Y. Zeng, J. Zheng, Z. Yang, M. Liao, S. Huang, B. Yan, J. Ye, Unraveling the passivation mechanisms of c-Si/ $\text{SiO}_x$ /poly-Si contacts, *Sol. Energy Mater. Sol. Cells* 250 (2023), 112047, <https://doi.org/10.1016/j.solmat.2022.112047>.
- [7] J. Stuckelberger, D. Yan, S.P. Phang, C. Samundsett, J. Wang, L. Antognini, F.-J. Haug, Z. Wang, J. Yang, P. Zheng, X. Zhang, D. Macdonald, Pre-annealing for improved LPCVD deposited boron-doped poly-Si hole-selective contacts, *Sol. Energy Mater. Sol. Cells* 251 (2023), 112123, <https://doi.org/10.1016/j.solmat.2022.112123>.
- [8] Q. Wang, K. Guo, L. Yuan, L. Li, H. Peng, B. Li, A. Wang, L. Zhang, W. Wu, J. Ding, N. Yuan, Boron tube diffusion process parameters for high-efficiency n-TOPCon solar cells with selective boron emitters, *Sol. Energy Mater. Sol. Cells* 253 (2023), 112231, <https://doi.org/10.1016/j.solmat.2023.112231>.
- [9] Y. Zhou, K. Tao, A. Liu, R. Jia, S. Jiang, J. Bao, S. Yang, Y. Cao, H. Qu, Study of boron diffusion for  $\text{p}^+$  emitter of large area N-type TOPCon silicon solar cells, *Appl. Phys. A* 126 (2020) 671, <https://doi.org/10.1007/s00339-020-03851-5>.
- [10] J. Hong, X. Liu, J. Ge, J. Sun, S. Liu, W. Yang, S. Jaffer, J. Lu, T. Qin, R. Chen, H. Shen, Superb improvement of boron doping in selective emitter for TOPCon solar cells via boron-doped silicon paste, *Sol. Energy* 247 (2022) 115–122, <https://doi.org/10.1016/j.solener.2022.10.031>.
- [11] J. Horzel, S. Mack, M. Meßmer, S. Schmidt, S. Richter, A. Wolf, J. Schön, J. Rentsch, in: On Retrograde Phosphorus Concentration Depth Profiles in Silicon after  $\text{POCl}_3$  Diffusion and Thermal Oxidation, 2022, 080002, <https://doi.org/10.1063/5.0089692>. Hamelin, Germany/Online.
- [12] X. Yang, J. Kang, W. Liu, X. Zhang, S. De Wolf, Solution-doped polysilicon passivating contacts for silicon solar cells, *ACS Appl. Mater. Interfaces* 13 (2021) 8455–8460, <https://doi.org/10.1021/acsami.0c22127>.
- [13] D. Ding, Z. Du, R. Liu, C. Quan, J. Bao, D. Du, Z. Li, J. Chen, W. Shen, Laser doping selective emitter with thin borosilicate glass layer for n-type TOPCon c-Si solar cells, *Sol. Energy Mater. Sol. Cells* 253 (2023), 112230, <https://doi.org/10.1016/j.solmat.2023.112230>.



- [14] H.P. Yin, W.S. Tang, J.B. Zhang, W. Shan, X.M. Huang, X.D. Shen, Screen-printed n-type Si solar cells with laser-doped selective back surface field, *Sol. Energy* 220 (2021) 211–216, <https://doi.org/10.1016/j.solener.2021.03.062>.
- [15] F. Haase, B. Lim, A. Merkle, T. Dullweber, R. Brendel, C. Günther, M. H. Holthausen, C. Mader, O. Wunnicke, R. Peibst, Printable liquid silicon for local doping of solar cells, *Sol. Energy Mater. Sol. Cells* 179 (2018) 129–135, <https://doi.org/10.1016/j.solmat.2017.11.003>.
- [16] Z. Kiaee, *Printed Dopant Sources for Locally-Doped SiO<sub>x</sub>/poly-Si Passivating Contacts*, 2018.
- [17] B. Pal, S. Ray, U. Gangopadhyay, P.P. Ray, Novel technique for fabrication of n-type crystalline silicon selective emitter for solar cell processing, *Mater. Res. Express* 6 (2019), 075523, <https://doi.org/10.1088/2053-1591/ab18ee>.
- [18] M. Ju, J. Park, Y.H. Cho, Y. Kim, D. Lim, E.-C. Cho, J. Yi, A novel method to achieve selective emitter using surface morphology for PERC silicon solar cells, *Energies* 13 (2020) 5207, <https://doi.org/10.3390/en13195207>.
- [19] N. Chhetri, G. Das, A. Kole, H. Saha, S. Haldar, S. Chatterjee, P-type polycrystalline silicon seed layer fabrication using RF-PECVD for thin film solar cells, *Mater. Today Proc* 58 (2022) 665–667, <https://doi.org/10.1016/j.matpr.2022.02.126>.
- [20] M. Stöhr, J. Aprojanz, R. Brendel, T. Dullweber, Firing-stable PECVD SiO<sub>x</sub>N<sub>y</sub>/n-Poly-Si surface passivation for silicon solar cells, *ACS Appl. Energy Mater.* 4 (2021) 4646–4653, <https://doi.org/10.1021/acsaem.1c00265>.
- [21] M. Firat, H. Sivaramakrishnan Radhakrishnan, M.R. Payo, P. Choulant, H. Badran, A. van der Heide, J. Govaerts, F. Duerinckx, L. Tous, A. Hajjiah, J. Poortmans, Large-area bifacial n-TOPCon solar cells with in situ phosphorus-doped LPCVD poly-Si passivating contacts, *Sol. Energy Mater. Sol. Cells* 236 (2022), 111544, <https://doi.org/10.1016/j.solmat.2021.111544>.
- [22] J. Stuckelberger, D. Yan, S.P. Phang, C. Samundsett, J. Wang, L. Antognini, F.-J. Haug, Z. Wang, J. Yang, P. Zheng, X. Zhang, D. Macdonald, Pre-annealing for improved LPCVD deposited boron-doped poly-Si hole-selective contacts, *Sol. Energy Mater. Sol. Cells* 251 (2023), 112123, <https://doi.org/10.1016/j.solmat.2022.112123>.
- [23] J.F. Mousumi, G. Gregory, J.P. Ganesan, C. Nunez, K. Provancha, S. Seren, H. Zunft, T. Jurca, P. Banerjee, A. Kar, R. Kumar, K.O. Davis, Process–structure–properties relationships of passivating, electron-selective contacts formed by atmospheric pressure chemical vapor deposition of phosphorus-doped polysilicon, *Phys. Status Solidi RRL – Rapid Res. Lett.* 16 (2022), 2100639, <https://doi.org/10.1002/pssr.202100639>.
- [24] S. Li, M. Pomaska, J. Hoß, J. Lossen, F. Pennartz, M. Nuys, R. Hong, A. Schmalen, J. Wolff, F. Finger, U. Rau, K. Ding, Poly-Si/SiO<sub>x</sub>/c-Si passivating contact with 738 mV implied open circuit voltage fabricated by hot-wire chemical vapor deposition, *Appl. Phys. Lett.* 114 (2019), 153901, <https://doi.org/10.1063/1.5089650>.
- [25] A. Ingenito, C. Allebé, S. Libraro, C. Ballif, B. Paviet-Salomon, S. Nicolay, J.J. Diaz Leon, 22.8% full-area bifacial n-PERT solar cells with rear side sputtered poly-Si(n) passivating contact, *Sol. Energy Mater. Sol. Cells* 249 (2023), 112043, <https://doi.org/10.1016/j.solmat.2022.112043>.
- [26] L. Nasebandt, B. Min, C. Hollemann, S. Hübner, T. Tippell, R. Peibst, R. Brendel, Sputtered phosphorus-doped poly-Si on oxide contacts for screen-printed Si solar cells, *Sol. RRL.* 6 (2022), 2200409, <https://doi.org/10.1002/solr.202200409>.
- [27] S.H. Sedani, O.F. Yasar, M. Karaman, R. Turan, Effects of boron doping on solid phase crystallization of in situ doped amorphous Silicon thin films prepared by electron beam evaporation, *Thin Solid Films* 694 (2020), 137639, <https://doi.org/10.1016/j.tsf.2019.137639>.
- [28] G.G. Untila, T.N. Kost, A.B. Chebotareva, ITO/SiO<sub>x</sub>/n-Si heterojunction solar cell with bifacial 16.6%/14.6% front/rear efficiency produced by ultrasonic spray pyrolysis: effect of conditions of SiO<sub>x</sub> growth by wet-chemical oxidation, *Sol. Energy* 204 (2020) 395–405, <https://doi.org/10.1016/j.solener.2020.04.076>.
- [29] Z. Liu, N. Lin, Q. Zhang, B. Yang, L. Xie, Y. Chen, W. Li, M. Liao, H. Chen, W. Liu, Y. Wang, S. Huang, B. Yan, Y. Zeng, Y. Wan, J. Ye, 24.4% industrial tunnel oxide passivated contact solar cells with ozone-gas oxidation nano SiO<sub>x</sub> and tube PECVD prepared in-situ doped polysilicon, *Sol. Energy Mater. Sol. Cells* 243 (2022), 111803, <https://doi.org/10.1016/j.solmat.2022.111803>.
- [30] H. Du, Z. Liu, W. Liu, M. Xiao, N. Lin, W. Yang, Q. Xia, M. Liao, B. Yan, Z. Yang, Y. Zeng, J. Ye, Concurrently preparing front emitter and rear passivating contact via continuous PECVD dposition plus one-step annealing for high-efficiency tunnel oxide Passivating contact solar cells, *Sol. RRL.* (2023), 2201082, <https://doi.org/10.1002/solr.202201082>.
- [31] B. Kaffle, B.S. Goraya, S. Mack, F. Feldmann, S. Nold, J. Rentsch, TOPCon-technology options for cost efficient industrial manufacturing, *Sol. Energy Mater. Sol. Cells* 227 (2021), 111100, <https://doi.org/10.1016/j.solmat.2021.111100>.
- [32] T.N. Truong, D. Yan, C.T. Nguyen, T. Kho, H. Guthrey, J. Seidel, M. Al-Jassim, A. Cuevas, D. Macdonald, H.T. Nguyen, Morphology, microstructure, and doping behaviour: a comparison between different deposition methods for poly-Si/SiO<sub>x</sub> passivating contacts, *Prog. Photovoltaics Res. Appl.* 29 (2021) 857–868, <https://doi.org/10.1002/ppp.3411>.
- [33] X. Yan, F.B. Suhaimi, M. Xu, J. Yang, X. Zhang, Q. Wang, H. Jin, V. Shanmugam, S. Duttgupta, Development of ultra-thin doped poly-Si via LPCVD and ex-situ tube diffusion for passivated contact solar cell applications, *Sol. Energy Mater. Sol. Cells* 209 (2020), 110458, <https://doi.org/10.1016/j.solmat.2020.110458>.
- [34] D.P. Pham, J. Yi, Dopant-grading proposal for polysilicon passivating contact in crystalline silicon solar cells, *J. Power Sources* 522 (2022), 231005, <https://doi.org/10.1016/j.jpowsour.2022.231005>.
- [35] Q. Wang, W. Wu, Y. Li, L. Yuan, S. Yang, Y. Sun, S. Yang, Q. Zhang, Y. Cao, H. Qu, N. Yuan, J. Ding, Impact of boron doping on electrical performance and efficiency of n-TOPCon solar cell, *Sol. Energy* 227 (2021) 273–291, <https://doi.org/10.1016/j.solener.2021.08.075>.
- [36] Q. Wang, W. Wu, N. Yuan, Y. Li, Y. Zhang, J. Ding, Influence of SiO<sub>x</sub> film thickness on electrical performance and efficiency of TOPCon solar cells, *Sol. Energy Mater. Sol. Cells* 208 (2020), 110423, <https://doi.org/10.1016/j.solmat.2020.110423>.
- [37] D. Ding, Z. Du, R. Liu, C. Quan, J. Bao, D. Du, Z. Li, J. Chen, W. Shen, Laser doping selective emitter with thin borosilicate glass layer for n-type TOPCon c-Si solar cells, *Sol. Energy Mater. Sol. Cells* 253 (2023), 112230, <https://doi.org/10.1016/j.solmat.2023.112230>.